



HAL
open science

Wave number determination of Pc 1-2 mantle waves considering He⁺⁺ ions: A Cluster study

B. Grison, C. Philippe Escoubet, O. Santolík, Nicole Cornilleau-Wehrin, Y. V. Khotyaintsev

► To cite this version:

B. Grison, C. Philippe Escoubet, O. Santolík, Nicole Cornilleau-Wehrin, Y. V. Khotyaintsev. Wave number determination of Pc 1-2 mantle waves considering He⁺⁺ ions: A Cluster study. *Journal of Geophysical Research Space Physics*, 2014, 119 (9), pp.7601-7614. 10.1002/2013JA019719 . hal-01552035

HAL Id: hal-01552035

<https://hal.science/hal-01552035>

Submitted on 11 Oct 2021

HAL is a multi-disciplinary open access archive for the deposit and dissemination of scientific research documents, whether they are published or not. The documents may come from teaching and research institutions in France or abroad, or from public or private research centers.

L'archive ouverte pluridisciplinaire **HAL**, est destinée au dépôt et à la diffusion de documents scientifiques de niveau recherche, publiés ou non, émanant des établissements d'enseignement et de recherche français ou étrangers, des laboratoires publics ou privés.



Distributed under a Creative Commons Attribution 4.0 International License

RESEARCH ARTICLE

10.1002/2013JA019719

Key Points:

- Direct measurement of EMIC wave number from refractive index method
- Unstable ion distribution functions in the plasma mantle close to the Earth
- Lack of ULF signature at the cusp magnetic footprint due to the cusp He^{++} resonance

Correspondence to:

B. Grison,
grison@ufa.cas.cz

Citation:

Grison, B., C. P. Escoubet, O. Santolík, N. Cornilleau-Wehrin, and Y. Khotyaintsev (2014), Wave number determination of Pc 1–2 mantle waves considering He^{++} ions: A Cluster study, *J. Geophys. Res. Space Physics*, 119, 7601–7614, doi:10.1002/2013JA019719.

Received 24 DEC 2013

Accepted 8 SEP 2014

Accepted article online 11 SEP 2014

Published online 30 SEP 2014

Wave number determination of Pc 1–2 mantle waves considering He^{++} ions: A Cluster study

B. Grison¹, C. P. Escoubet², O. Santolík^{1,3}, N. Cornilleau-Wehrin^{4,5}, and Y. Khotyaintsev⁶

¹Institute of Atmospheric Physics, ASCR, Prague, Czech Republic, ²ESA/ESTEC, RSSD, Noordwijk, Netherlands, ³Charles University, Prague, Czech Republic, ⁴LPP/CNRS, Polytechnique, Palaiseau, France, ⁵LESIA, Observatoire de Meudon, France, ⁶IRFU, Uppsala, Sweden

Abstract The present case study concerns narrowband electromagnetic emission detected in the distant cusp region simultaneously with upgoing plasma flows. The wave properties match the usual properties of the Pc 1–2 mantle waves: small angle between the wave vector and the magnetic field line, left-hand polarization, and propagation toward the ionosphere. We report here the first direct wave vector measurement of these waves (about 1.2×10^{-2} rad/km) through multi spacecraft analysis using the three magnetic components and, at the same time, through single spacecraft analysis based on the refractive index analysis using the three magnetic components and two electric components. The refractive index analysis offers a simple way to estimate wave numbers in this frequency range. Numerical calculations are performed under the observed plasma conditions. The obtained results show that the ion distribution functions are unstable to ion cyclotron instability at the observed wave vector value, due to the large ion temperature anisotropy. We thus show that these electromagnetic ion cyclotron (EMIC) waves are amplified in the distant cusp region. The Poynting flux of the waves is counterstreaming with respect to the plasma flow. This sense of propagation is consistent with the time necessary to amplify the emissions to the observed level. We point out the role of the wave damping at the He^{++} gyrofrequency to explain that such waves cannot be observed from the ground at the cusp foot print location.

1. Introduction

The in situ detection of magnetosheath ions in the terrestrial polar cusps has revealed a direct access of shocked solar wind ions to the ionosphere [Heikkilä and Winningham, 1971; Frank, 1971; Russell et al., 1971]. Only part of the injected plasma flow reaches the ionosphere (downward). The other part is mirrored, due to the increasing magnetic field, and is flowing away from the ionosphere (upward). The structure of the cusps depends mainly on the orientation of the z component of the Interplanetary Magnetic Field (IMF) [e.g., Burch, 1973; Reiff et al., 1980; Carbary and Meng, 1986; Escoubet and Bosqued, 1989; Lavraud et al., 2005; Escoubet et al., 2008]. Under a northward IMF ($B_{IMFz} > 0$) the injection site is located on the magnetopause poleward of the cusp. Mirrored ions are found on opened magnetic field lines forming the stagnant cusp and on closed field lines after being reconnected on both hemispheres. Under a southward IMF ($B_{IMFz} < 0$) the reconnection site is located on the dayside magnetopause. The mirrored ions are then flowing tailward on open field lines also called the plasma mantle after Rosenbauer et al. [1975]. At low altitude plasma mantle definition has been based on the mean ion energy [Newell and Meng, 1992]. However, given the high-altitude Cluster observations, we prefer to follow here the definition given in Engebretson et al. [2005]: the mantle is the region where the plasma flows upward and the cusp proper is the region where the plasma flows downward. This definition is easier to handle when observations take place in the distant cusp region where mantle and cusp proper are adjacent to each other.

Since the early in situ measurements [Russell et al., 1971; Scarf et al., 1972] electromagnetic ion cyclotron (EMIC) waves are known to be recurrent features of the Earth's magnetosphere polar cusps. HEOS-2 data revealed simultaneity of downward ion flows and ultra-low-frequency (ULF) magnetic noise in the high altitude cusp region [D'Angelo et al., 1974]. These observations have been confirmed by Polar observations [Le et al., 2001] and Cluster observations [Nykyri et al., 2004, 2006; Grison et al., 2005]. These waves, probably due to their large perpendicular wave vector component [Grison et al., 2005; Sundkvist et al., 2005a], do not propagate to the ground [Engebretson et al., 2009]. Several local mechanisms explain the wave generation in the cusp: velocity shears [Le et al., 2001; Nykyri et al., 2004], current instabilities

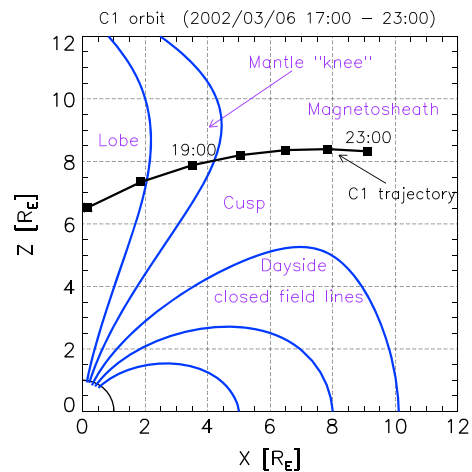


Figure 1. Schematic layout of Cluster-1 orbit between 17:00 and 23:00 (06/03/2002) projected in the $(X-Z)_{GSE}$ plane. Spacecraft location is marked every hour. Geomagnetic field lines (in blue) are computed for the K_p index value (4) observed that day between 18:00 and 21:00.

[Grison *et al.*, 2005], and the proton shell distribution functions [Sundkvist *et al.*, 2005b]. Broadband emissions can also propagate into the cusp from the magnetosheath [Sundkvist *et al.*, 2005a].

On ground Pc 1–2 waves [Jacobs *et al.*, 1964] are observed poleward to the cusp boundary [Menk *et al.*, 1992; Engebretson *et al.*, 2009]. Dyrud *et al.* [1997] first proposed that these waves can be generated by mirrored ions in the polar mantle, just tailward of the cusp. The inferred source location displays a shallow minimum in the polar mantle magnetic field, and it can be described as the “knee” of the mantle (after Figure 10 in Dyrud *et al.* [1997] and after Engebretson *et al.*, 2005). Direct observations of Pc 1–2 waves in the plasma mantle adjacent to the cusp support that hypothesis [Engebretson *et al.*, 2005]. In the region of these Polar case studies, about 6–7 Earth radii (R_E , 6371 km), the distribution functions are stable to the ion cyclotron instability, and the authors therefore conclude that waves are generated at higher altitude.

The observed waves, so-called mantle waves, are narrowband with a clear left-hand polarization and a small propagation angle ($\sim 20^\circ$). These waves can then be observed in the distant mantle simultaneously with unstable distribution functions to the ion cyclotron instability [Engebretson *et al.*, 2012]. Such distribution function has not been reported yet below the mantle “knee”.

In the present study we show a distant cusp crossing by the spacecraft fleet of the Cluster mission [Escoubet *et al.*, 2001] at about $9 R_E$ from the Earth. After the description of the instrumentation, we show an overview of the cusp crossing and the interplanetary conditions. We focus our analysis on narrowband emissions found in conjunction with upward plasma flows. Among the wave properties the wave vector is determined through single and multi-spacecraft techniques. The results are compared to wave stability analysis performed through WHAMP (Waves in Homogeneous, Anisotropic Multi-component Plasmas) code [Rönmark, 1982] using the locally observed distribution functions. We finally discuss our results and the possibility for the distant cusp to be the source region of the Pc 1–2 waves observed in the plasma mantle and on the ground.

2. Instrumentation

We used data from several instruments onboard Cluster. The 25 Hz sampled temporal series of the electromagnetic fluctuations are provided by the STAFF instrument [Cornilleau-Wehrlin *et al.*, 2003] for the magnetic part and by the EFW instrument [Gustafsson *et al.*, 2001] for the electric part. The ambient vector magnetic field (hereafter called \mathbf{B}_0) is estimated with a 4 s resolution from the prime parameters of the FGM instrument [Balogh *et al.*, 2001]. Ion properties are given by the CIS/HIA and CIS/CODIF instruments at a 4 s resolution [Rème *et al.*, 2001]. For our WHAMP study we also use the electron moments provided by the PEACE instrument [Johnstone *et al.*, 1997]. MAG [Smith *et al.*, 1998] and SWEPAM [McComas *et al.*, 1998] instruments onboard ACE spacecraft provide IMF components and solar wind composition measurements. ACE data propagated to the bow shock nose are provided by OMNIWeb Plus at NASA/GSFC at a 1 min resolution.

3. Observations

3.1. Three Hour Overview

The Cluster fleet crossed the distant part of the northern cusp region on 6 March 2002. The present study deals with that crossing. Since the inter-spacecraft separation is small (the minimum separation is 80 km, the maximum 120 km) we only show Cluster-1 (C1) projected orbit in Figure 1. Ambient magnetic field lines have been computed using the T89 model [Tsyganenko, 1989]. This model requires K_p index value as input. Between 18:00 and 21:00 UT (hereafter given times always refer to the Universal Time), K_p value is 4,

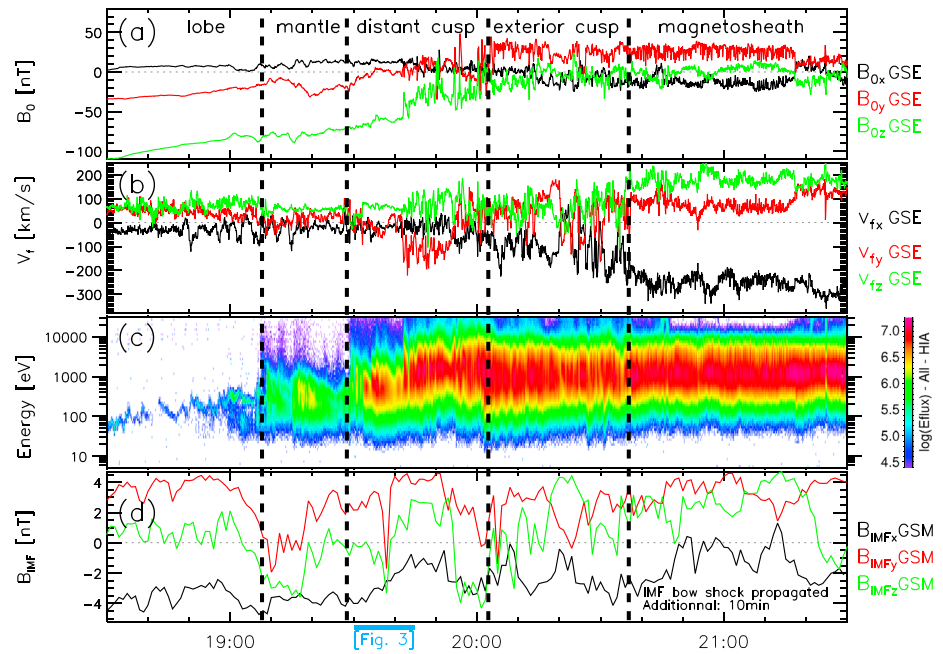


Figure 2. Three hour overview of the cusp crossing by C1 (panels a, b, and c) and of the lagged IMF (panel d). Vertical dashed lines delimitate the different regions crossed by the spacecraft.

indicative of a strong geomagnetic activity. C1 successively encounters the lobe of the magnetosphere, the distant cusp region, and the magnetosheath. The entry into the magnetosheath is expected to occur around 21:00. The outbound crossing of the cusp region takes place on the poleward side of the cusp. Figure 2 presents C1 and ACE data, from top to bottom: B_0 , the flow velocity and the ion flux energy diagram between 18:30 and 21:30. The IMF from ACE (propagated to the bow shock nose) is plotted on panel d. IMF data are shifted by additional 10 min to take into account the propagation delay from the bow shock to the cusp region. This delay is consistent with observations in the cusp region [Escoubet et al., 2013]. Times are given hereafter with a 1 min precision which is the lowest time resolution of the plotted data. At 19:30 the spacecraft position is $(4.3 R_E; 2.8 R_E; 8.1 R_E)_{GSE}$. The vertical dashed lines on Figure 2 delimitate the main regions crossed by C1.

Before 19:08, in the lobe, one can notice the dipolar evolution of the magnetic field (Figure 2a) and the low ion flux (Figure 2c) with possible oxygen outflows [Liao et al., 2010 and references therein]. The presence of upgoing oxygen ions is confirmed by the CIS/CODIF measurements (not shown). Then the flux intensity progressively increases until 20:03 in the energy range 0.1 – 10 keV which is typical for magnetosheath-origin ions (Figure 2c). Between 19:08 and 19:42, the flow velocity \mathbf{v}_f is mainly antiparallel to \mathbf{B}_0 (hereafter parallel and perpendicular without any precisions refer to \mathbf{B}_0 orientation) indicative of upgoing plasma. This direction is deduced from consideration on the sign of each component of \mathbf{B}_0 and \mathbf{v}_f . It is more clearly shown in the next section. After 19:42 \mathbf{B}_0 is more depressed and it varies a lot. At the same time the flow velocity is highly variable. The high-energy ion cutoff, below 1 keV, observed on the upgoing plasma (19:08–19:28) is characteristic of the formation of a plasma mantle population [Rosenbauer et al., 1975]. We can thus consider that the spacecraft is in the distant cusp starting from 19:28. After 19:42, the ion energy level and the sharp variations of the flow velocity (mainly along v_{fy}) correspond to signatures of ion injections in the cusp [Russell et al., 1971; Le et al., 2001]. Between 20:03 and 20:37 the flow velocity varies abruptly in orientation and in intensity, the ion energy is magnetosheath-like, and the magnetic field orientation is almost constant. After 20:37, the flow velocity (Figure 2b) has a constant orientation: negative v_{fx} (in black), positive v_{fz} (in green), and low v_{fy} (in red). The flow skirts around the magnetosphere with a typical energy of a shocked solar wind: the spacecraft is in the magnetosheath. The magnetosheath-like magnetic field together with the flow direction highly deviated from the magnetosheath mean flow observed between 20:03 and 20:37 match the exterior cusp definition by Chen et al. [1997]. The magnetopause definition and location in the exterior cusp vicinity are complex topics, even under steady IMF conditions [Russell, 2000; Lavraud et al., 2002,

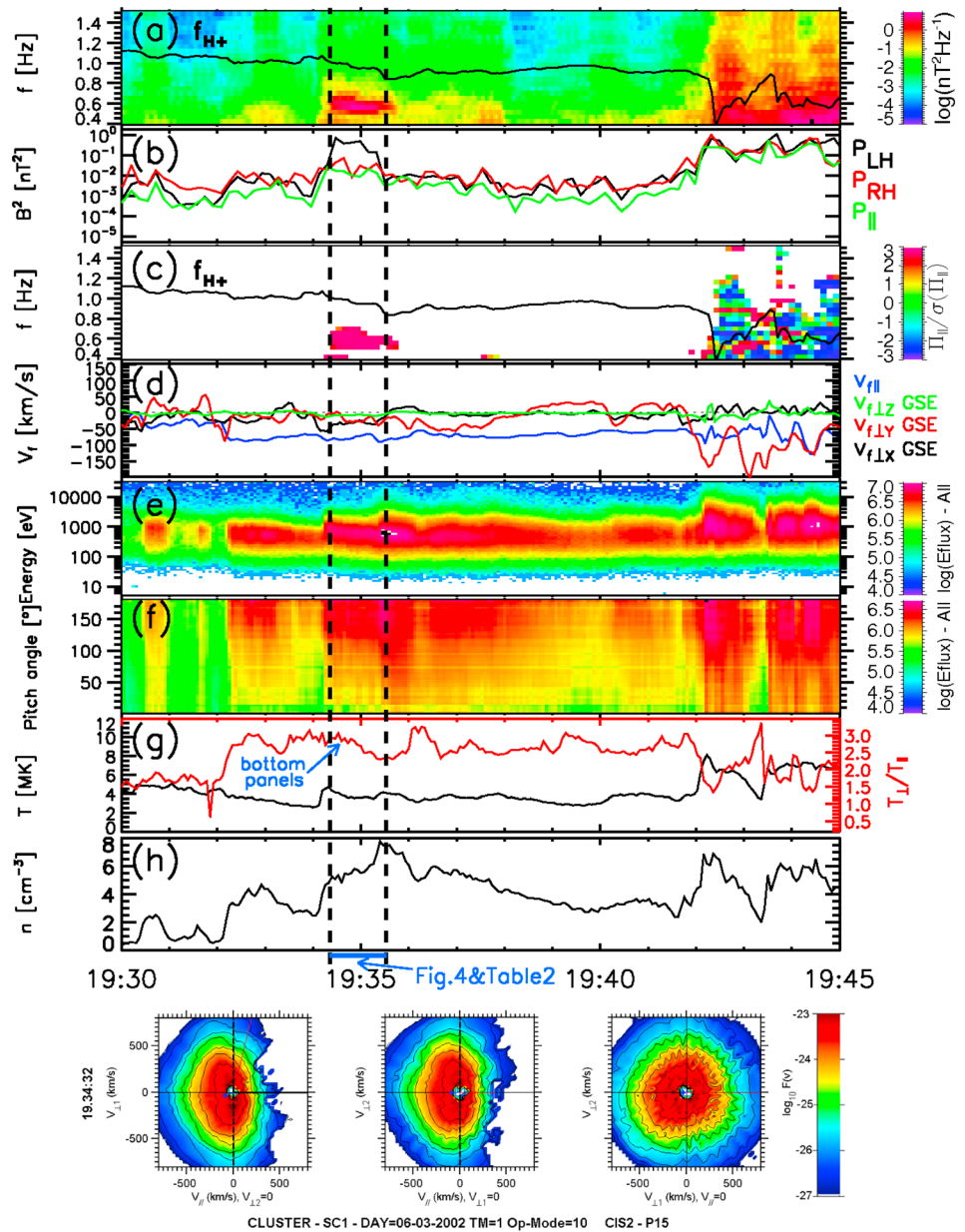


Figure 3. Top panels: 15 min overview of Cluster data: (a) the magnetic power spectral density; (b) three components of the integrated magnetic power; (c) positive (red) or negative (blue) values of the normalized parallel component of the Poynting flux indicate a field aligned or anti-field aligned propagation, respectively; ion flux is plotted with respect to the energy (d) and the pitch angle (e); (f) the ion temperature is shown in black with the left-hand axis scale and the temperature anisotropy is plotted in red with the right-hand axis scale; and (g) the ion density. Bottom: cuts in three planes of the 3D ion distribution functions obtained over 4 s.

2004]. The absence of abrupt rotation in \mathbf{B}_0 orientation in the present case indicates that the spacecraft does not encounter the magnetopause as a rotational discontinuity. The spacecraft might thus be located on reconnected field lines. We can also note the disturbed aspect of the magnetosheath (detection of ions with energy larger than 10 keV). The magnetopause is not clearly identified during this outbound crossing; nevertheless, it is certain that between 19:28 and 20:03 the spacecraft are in the distant cusp region with some features of plasma mantle formation at the beginning.

Polar cusp location and structure are very sensitive to the IMF orientation, especially to the sign of B_{IMFz} [e.g., Burch, 1973; Reiff et al., 1980; Carbary and Meng, 1986; Escoubet and Bosqued, 1989; Pitout et al.,

2006b; Escoubet *et al.*, 2008]. Under northward IMF (respectively, southward), ion injections are expected close to the lobe-cusp boundary (resp. close to dayside closed field lines-cusp boundary), and stagnant plasma flows (resp. upgoing flows) are detected away from this boundary. The IMF (Figure 2d) is most of the time dominated by a positive $B_{IMF y}$ (in red) and a negative $B_{IMF x}$ (in black). $B_{IMF z}$ (in green) sign frequently changes. During the mantle and the cusp crossings by C1, $B_{IMF z}$ is positive between 19:39 and 19:53. Even if the cusp has a quick response to a $B_{IMF z}$ change [Vonrat-Reberac *et al.*, 2003; Escoubet *et al.*, 2008; Pitout *et al.*, 2006a], it usually needs more than 20 min to fully adapt to an IMF orientation change [Pitout *et al.*, 2006b]: quick changes in the IMF orientation make unlikely the observations of all the usual cusp features that are described for steady interplanetary conditions. It is therefore difficult to make clear predictions for the whole cusp crossing. The long period (≈ 35 min) of an almost steady southward IMF before 19:39 is consistent with the observations of plasma mantle by C1. The ion injections seen after 19:42 might be related to the period of slightly northward IMF observed between 19:39 and 19:53. These variations in the $B_{IMF z}$ sign might explain also why injection signatures follow mantle-like plasma detection within a short time interval (19:40:19:45), the poleward cusp boundary being characteristic for these two populations under the two opposite orientations of $B_{IMF z}$.

3.2. Fifteen Minute Overview

Let us now concentrate on Cluster data during the time of the wave event we are interested in. Figure 3 presents Cluster-1 wave and particle data and Cluster-4 (C4) Poynting flux measurements between 19:30 and 19:45, when in the distant cusp. Data are provided by the STAFF-SC, EFW, CIS-HIA, and FGM instruments, respectively, for the magnetic and electric fluctuations, ion properties, and ambient magnetic field. We plot from top to bottom: the time-frequency diagram (spectrogram) of the total magnetic power spectral density (PSD) with the local proton gyrofrequency (f_{H+}) overplotted in black (Figure 3a), the three components of the integrated (0.4–10 Hz range) magnetic power (Figure 3b), the spectrogram of the parallel component of the normalized Poynting flux (Figure 3c), the three GSE components of the perpendicular ion bulk velocity and the parallel velocity (Figure 3d), the ion flux intensity as a function of time and energy (Figure 3e), the ion flux intensity as a function of time and pitch angle (Figure 3f), the ion total temperature (in black), and the ion temperature anisotropy (T_{\perp}/T_{\parallel} , in red) on panel g and the ion density (Figure 3h). The three integrated components of the wave magnetic power are calculated in a magnetic field aligned reference frame giving polarized power in the plane perpendicular to \mathbf{B}_0 (left and right handed) and parallel to \mathbf{B}_0 . The three bottom panels represent the cuts in three planes of the ion distribution function obtained over 4 s during the wave event at 19:34:32.

We first comment on the magnetic wave activity. The spectrogram (Figure 3a) has been computed using a fast Fourier transform (FFT). There are 512 points per FFT window with an overlap of 90% between two consecutive windows. This gives a smooth evolution of the magnetic wave activity. The integrated power (Figure 2b) has been computed using 256 point FFT windows with no overlap. This shows more precisely when the magnetic activity starts rising or decreasing. One can notice a 1 min peak starting from 19:34:20 centered around 0.55 Hz, below f_{H+} . The structure is delimited by the two vertical black dashed lines. The left-handed (LH, in black) component of the wave power is more than 10 times higher than the two others indicative of a strong degree of left-handed circular polarization. We can refer to this structure as to an EMIC wave [Horne and Thorne, 1993].

The parallel component of the Poynting flux (Π_{\parallel}) normalized by its standard deviation ($\sigma(\Pi_{\parallel})$) is computed from the three components of the wave magnetic field (\mathbf{B}) and the two components of the wave electric field (\mathbf{E}) after the method proposed by Santolik *et al.* [2001]. This method is based on the phase shift estimation between \mathbf{E} and \mathbf{B} in the frequency domain. It leads to an approximate estimation of Π_{\parallel} from the real parts of the cross spectra between each electric component and the two perpendicular magnetic components. The absolute value of $\Pi_{\parallel}/\sigma(\Pi_{\parallel})$ indicates the reliability of the results, and the best results are obtained for a single planar wave. The displayed values on Figure 3c are averaged over 10 consecutive time intervals. Positive (respectively, negative) values indicate a parallel (respectively, anti-parallel) Poynting flux orientation. For a given time and a given frequency bin, Poynting flux values displayed are limited to the high magnetic power density values (values larger than 0.1 nT²/Hz). This high energy filter highlights a cutoff of the electromagnetic energy at 0.5 Hz when the upper boundary of the structure varies. Positive values observed here (2–3) for the EMIC emission indicate that the electromagnetic energy is aligned with the magnetic field, i.e., it propagates toward the ionosphere.

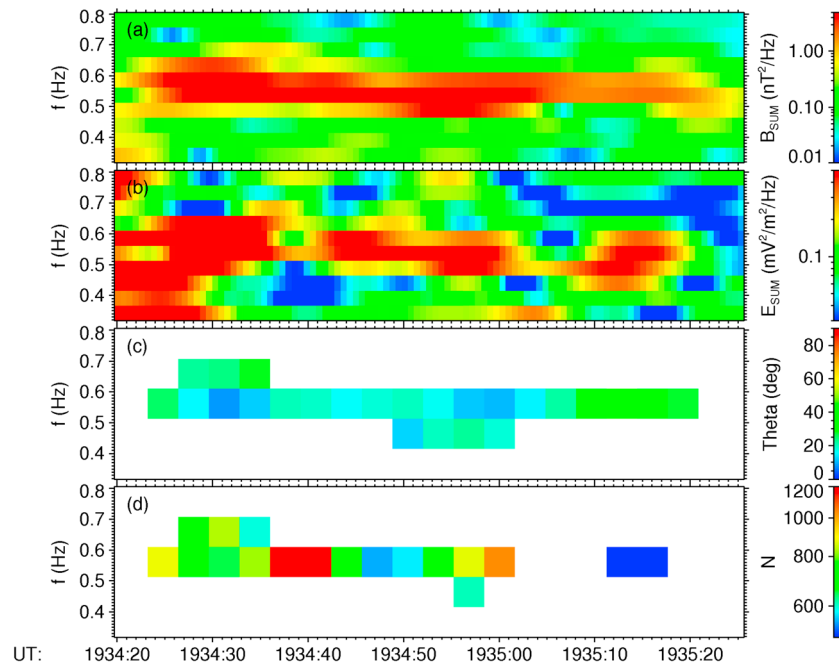


Figure 4. Focus on the electromagnetic ion cyclotron (EMIC) waves. Magnetic (resp. electric) power spectral density (PSD) spectrogram is plotted on panel a (resp. b). The blue values of the propagation angle (panel c) indicate a field aligned angle. The propagation angle (\mathbf{k}, \mathbf{B}_0) and N ($=n/Z$, panel d) values are plotted only for the most intense part of the emissions. The mean values are: $(\mathbf{k}, \mathbf{B}_0) = 20^\circ$ and $N = 775$.

The second episode of enhanced wave activity takes place after 19:42. The mean level of magnetic fluctuations increases, the three components being this time roughly of the same intensity and $\Pi_{\parallel}/\sigma(\Pi_{\parallel})$ does not indicate any clear direction. This is the signature of typical broadband emissions in the cusp [Grison et al., 2005; Sundkvist et al., 2005b].

The ion flow is upgoing during the 15 min as indicated by the negative values of the parallel bulk flow velocity (Figure 3d, $v_{f\parallel}$). $v_{f\parallel}$ is generally larger than the perpendicular velocities until 19:42. Peaks of the perpendicular velocity ($v_{f\perp y}$) are observed at the beginning of the presented time interval, but the ion flux is very low at that time (Figure 3e). Large peaks also occur at the end of the interval (19:42–19:45) when the field aligned ion fluxes are the most intense (Figure 3f). These magnetosheath ion injections occur on newly reconnected field lines: as the IMF is mainly duskward (cf. Figure 2d), one expects a dawnward convection of recently opened field lines in the cusp, as observed here ($v_{f\perp y} < 0$) [Gosling et al., 1991; Lavraud et al., 2005]. These events are coincident with large wave activity (Figure 3c). The wave activity detected after 19:42 is thus linked with recent ion injections and velocity shears: this is usual for broadband wave activity in the cusp region [D’Angelo et al., 1974; Grison et al., 2005; Nykyri et al., 2006]. $v_{f\perp x}$ turns positive after 19:42: reconnection occurs for these injections from the magnetopause lobeside [Dungey, 1961; Lavraud et al., 2005].

The flux level (Figure 3e) intensifies after 19:32. The mean energy increases step by step: 19:32:00, 19:34:00, and 19:35:30 and then decreases slowly until 19:42 where a sharp increase is observed, with a mean energy of 800 eV. It is usual observations for Cluster outbound cusp crossing under southward IMF: the spacecraft encounters first mirrored ion fluxes that progressively get more energetic and more intense [Lavraud et al., 2005]. Then, the spacecraft enters the injection region at 19:42. The monochromatic EMIC emission seen just after 19:34 is detected during a period of upgoing plasma without neither ion injections nor velocity shears. This narrowband emission cannot be related in this case with velocity shears nor with unidirectional ion flow toward the ionosphere as previously reported [Le et al., 2001; Nykyri et al., 2003; Nykyri et al., 2004]. The simultaneously detected upgoing plasma flow leads us to identify these waves as Pc 1–2 mantle waves [Engebretson et al., 2005]. The ion average temperature (Figure 3g) is about 4 MK before 19:42 and it rises to 6 MK later. The temperature anisotropy ratio is about 2.5–3 before the injections, and later it is lower. The anisotropy is clearly shown on the bottom panels of Figure 3 that presents ion distribution function cuts

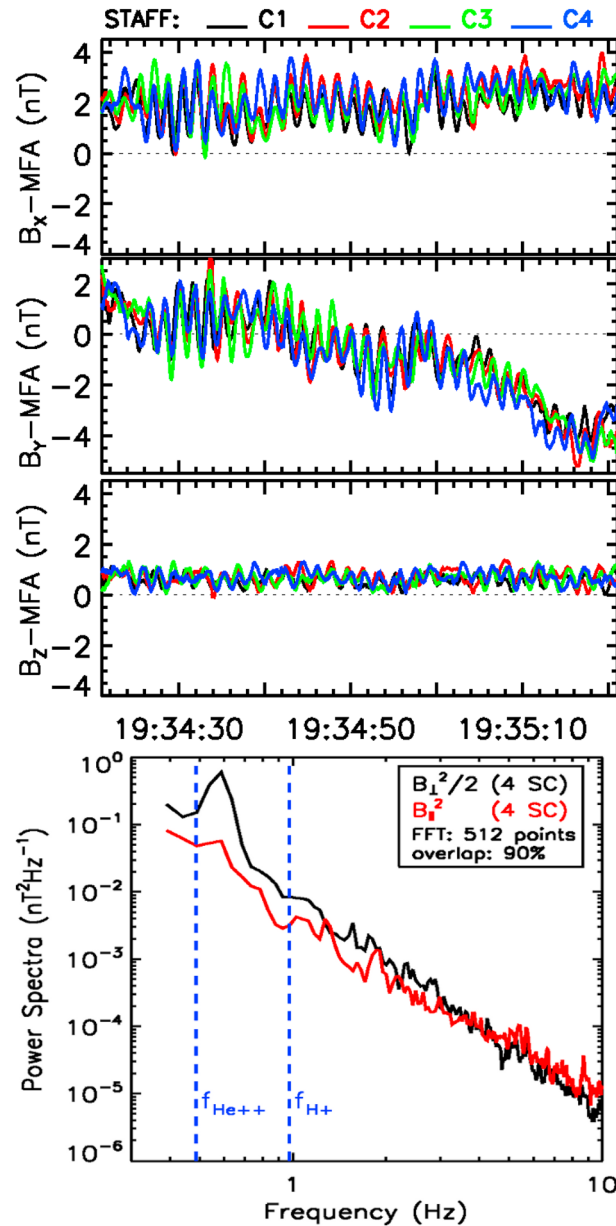


Figure 5. Top: Three components of the magnetic waveform of the four spacecraft in MFA coordinate system. Bottom: Total magnetic spectra (over the 4 spacecraft) of the transverse (black) and parallel (red) fluctuations.

the interface between the electric antennas and the plasma. We thus determine in practice $N = n/Z$. In our case of low-frequency waves we assume $Z = 1$ (and $N = n$), assumption that we discuss later on. The singular value decomposition (SVD) method is used to determine κ [Santolik et al., 2003]. This method takes into account all information contained in a spectral matrix. The 180° ambiguity in the \mathbf{k} orientation resulting from single spacecraft method is resolved by taking into account the positive parallel component of the Poynting vector (Figure 3c).

The resulting wave vector angle (\mathbf{k}, \mathbf{B}_0) is shown in Figure 4c where values are averaged over 10 neighboring samples (5 in time and 2 in frequency). Considering only the values where the total magnetic PSD is larger than 0.85 nT²/Hz (other are discarded and drawn in white), (\mathbf{k}, \mathbf{B}_0) is mostly lower than 30°. The average and standard deviation of the propagation angle are $(\mathbf{k}, \mathbf{B}_0) = 20^\circ \pm 8^\circ$. The results for n (or N) are shown in

in the two $v_{\parallel} - v_{\perp}$ planes and in the $v_{\perp} - v_{\perp}$ plane. One can notice an isotropic distribution in the $v_{\perp} - v_{\perp}$ plane when the distribution function is larger in both perpendicular directions than in the parallel one. The influence of the high temperature anisotropy on the wave growth is discussed in section 4. Finally, the ion density (Figure 3h) is maximal ($n > 4 \text{ cm}^{-3}$ and up to 8 cm^{-3}) when the intense EMIC waves are detected.

3.3. Wave Number Determinations (1 Min Zoom on the Wave Structure)

3.3.1. Single Spacecraft Analysis

In Figure 4 we focus on the time interval delimited by the dotted lines in Figure 3. It is the same time interval that is used for the forthcoming multispacecraft analysis. Spectrograms of the wave electric (Figure 4a) and wave magnetic (Figure 4b) fields have been computed with a 512 points sliding window FFT. The overlap between two consecutive windows is about 90%. It highlights the electric component of the previously observed EMIC waves. The wave number k can be estimated from multicomponent measurements of magnetic and electric wavefields on a single spacecraft using the refractive index n of the waves, $k = n \omega/c$, where ω is the wave angular frequency, and c is the speed of light. n can be determined using the Faraday's law in the frequency domain: $n(\kappa \wedge \mathbf{E}) = c\mathbf{B}$, where κ is the wave vector direction ($\kappa = \mathbf{k}/k$). n can be achieved from measurements of three orthogonal magnetic search coils and two electric antennas (equations (10) and (11) in Santolik et al. [2001]). This method is similar to the one used to compute Π_{\parallel}/σ (Π_{\parallel}). Antennas provide \mathbf{E}/Z measurements, where Z is the complex transfer function of

Table 1. Spacecraft Positions in MFA Reference Frame Relatively to the Tetrahedron Mesocenter (in km)

	X	Y	Z
C1	12.0	-17.3	-51.0
C2	-4.5	39.4	5.5
C3	-63.9	-11.3	23.7
C4	56.3	-10.9	21.8

Figure 4d. In addition to the threshold on the magnetic PSD, we consider only the electric PSD values larger than $0.25 \text{ V}^2 \text{ m}^{-2} / \text{Hz}$. This additional threshold explains why the regions of nonzero values are different for N and $(\mathbf{k}, \mathbf{B}_0)$. n varies between 500 and 1100, the average value and standard

deviation being $n = 775 \pm 285$. Considering $k = n \omega / c$, we obtain $k = 9.4 \times 10^{-3} \pm 3.5 \times 10^{-3} \text{ rad/km}$ (taking $\omega = 2\pi \times 0.58 \text{ rad/s}$). The standard deviation is about one third of the mean value. Looking at Figure 4d one can notice large n values at 19:34:40. At the same time the electric PSD is very low. Similarly at 19:35:15 n turns to small values when the magnetic PSD is a bit weaker than previously. On the one hand it means that this method can resolve short duration changes (at 19:35:15); on the other hand, one must be careful to consider time intervals when both electric and magnetic PSD are sufficiently intense.

3.3.2. Multi Spacecraft Analysis

Let us now consider waveform data from the four Cluster spacecraft. Top panels of Figure 5 present the three components of the magnetic waveforms measured by the four STAFF-SC instruments, from top to bottom B_x , B_y , and B_z in the magnetic field aligned (MFA) coordinate system. The total duration is about 1 min, starting at 19:34:20, which is the duration of the wave event, and the MFA system has been defined using the average value of \mathbf{B}_0 measured on each spacecraft during a wider time interval of 3 min to estimate the ambient magnetic field, as done in a previous study [Grison *et al.*, 2005]; that is why the B_x and B_y curves are not centered on 0 (dashed line). In the GSE coordinate system, $\mathbf{B}_0 = (14.9; -3.7; -63.0) \text{ nT}$ and $|\mathbf{B}_0| = 64.9 \text{ nT}$. After 19:35, the mean value of the B_y waveform decreases from 0 nT to -4 nT, indicative of a small change of \mathbf{B}_0 along this component. In order to compare fluctuation amplitudes, the same range size (8.5 nT) is used on the three panels. Larger oscillations are observed along B_x and B_y , than along B_z , confirming the transverse polarization of the waves (cf. Figure 3b). The maximal peak to peak amplitude is 4 nT (6% of $|\mathbf{B}_0|$) and the oscillation amplitudes are weaker at the end of the time interval. The fluctuations are sinusoidal-like with a period slightly shorter than 2 s (2 s = one minor tick interval), and they are seen at the four spacecraft. The small inter-spacecraft separations (cf. Table 1) explain why the four satellites observe similar magnetic structures.

To precisely estimate the oscillation frequency, we compute the spectrum (Figure 5, bottom panel) of the magnetic power density during this period (1200 points per component per spacecraft) using a FFT with a sliding window of 512 points and 90% overlap between two windows along each component. The displayed frequency interval varies from 0.35 to 10 Hz. For each component, spectra are summed over all spacecraft and the two perpendicular components (x and y) are averaged. The black curve represents one half of the power density of the transverse magnetic fluctuations, and the red curve shows the parallel power density. In addition to the transverse nature of the fluctuations, this plot confirms the monochromatic aspect of the structure, the spectrum being dominated by a single peak that maximizes just below 0.6 Hz (no harmonics are seen). Two vertical dashed lines indicate the local proton gyrofrequency ($f_{H^+} = 0.97 \text{ Hz}$) and the local He^{++} gyrofrequency ($f_{\text{He}^{++}} = f_{H^+}/2$). As f_{H^+} is very close to 1 Hz, further frequency considerations can almost equally refer to absolute frequencies and frequencies normalized to f_{H^+} . The observed peak starts close to $f_{\text{He}^{++}}$, and it does not spread up to f_{H^+} . We recall here that these frequencies are given in the spacecraft frame.

Table 2. Experimental Results (Multi-spacecraft Analysis)^a

$f_{sc \text{ frame}}^*$	E_{max}	k	k^*	$\theta(\mathbf{B}_0, \mathbf{k})$	$f_{\text{plasma frame}}^*$
0.48	0.02	0.011	0.29	18.2	0.63
0.53	0.09	0.011	0.29	18.2	0.68
0.57	0.08	0.012	0.33	15.9	0.74
0.61	0.02	0.012	0.32	7.2	0.76

^aFor each of the four normalized spectral frequencies (f/f_{H^+}) in the spacecraft frame (col.1), we give values of the maximal energy density (col.2 in $\text{nT}^2/\text{Hz}/(\text{rad/km})^3$), of the corresponding absolute and normalized (k_p) wave numbers (col. 3 in rad/km and col.4), of the propagation angle (col. 5 in degrees), and of the normalized frequency in the plasma frame (Doppler corrected) of this maxima (col. 6).

Table 3. Observed Parameters for the Numerical Calculations ($\mathbf{B}_0 = 64$ nT and $\theta(\mathbf{B}_0, \mathbf{k}) = 15^\circ$)

Species	n (cm^{-3})	T_{\parallel} (eV)	T_{\perp}/T_{\parallel}
H^+	5.7	240	2.8
He^{++}	0.19	1200	1.
e^-	6.08	41	1.13

As the Cluster fleet is in a close configuration, we apply the k-filtering analysis [Pinçon and Lefeuvre, 1991; Pinçon and Motschmann, 1998]. The k-filtering technique is based on the simultaneous measurements of a given wavefield in several points of space. It allows one to estimate the energy distribution function of this wavefield in the 4-D Fourier space (\mathbf{k}, ω). The method adopts a plane wave decomposition. The hypotheses of time stationarity and space homogeneity of the signal are not strictly fulfilled in real data. However, in practice, we are content with a homogeneous (stationary) signal on scales that are larger than the largest spatial (temporal) scale determined by the k-filtering method. This technique which has been first used in the magnetosheath by Sahraoui et al. [2003] takes all advantages of the four points of measurements. The assumptions of the method are fulfilled in the present case. The fleet is in a pseudo-spherical configuration (tetrahedron elongation = 0.31 and planarity = 0.28), the medium is homogeneous, and the conditions are almost stationary: signals of the four spacecraft look alike, and there are almost 30 periods in the studied window. Moreover, the present plasma environment is more stable in the present case than during a previous successful application of the method in the cusp region [Grison et al., 2005]. Table 2 presents in column 2 the location of the energy density maximum (in $\text{nT}^2/\text{Hz}/(\text{rad}/\text{km})^3$) in the Fourier space for each of the peak spectrum normalized frequencies, i.e., 0.48, 0.53, 0.57, and 0.63 Hz. As expected, the maximum is larger in the peak central frequencies (0.53 and 0.57 Hz). The wave number has similar values for all the studied frequencies (columns 3 and 4) with a slight increase with frequency: $k \approx 1.15 \times 10^{-2}$ rad/km in average. The propagation angle is inclined by about 15° with respect to \mathbf{B}_0 (column 5). The variability in the angle results from a low spatial resolution. Multiplying k by the proton Larmor radius (ρ , 28 km) we obtain the normalized parameter $k^* \approx 0.3$. Because of the low propagation angle, we considered the mean parallel ion temperature (≈ 155 eV) given by the CIS/HIA instrument to calculate ρ . Assuming that the waves are embedded in the plasma flow, we can remove the Doppler shift to get the frequency in the plasma frame (column 6). The peak has a similar width as in the

spacecraft frame, but it is centered on a larger frequency (0.70 Hz instead of 0.55 Hz). It is now clearly above $f_{\text{He}^{++}}$ but still below f_{H^+} . These properties agree with the SVD analysis applied on single spacecraft data: the wave vector is almost aligned with \mathbf{B}_0 and both the k-filtering analysis and the refractive index analysis provide similar wave number values. The pros of the k-filtering analysis are that the wave vector is estimated from the magnetic waveform only and there is no need to state $Z = 1$. However the refractive index analysis requires single spacecraft measurements only, and it seems to offer a good temporal resolution. The single spacecraft analysis is valid and gives significant results in the present case, as only one plasma wave mode is present at a given frequency in the spacecraft frame.

3.3.3. Stability Analysis

In solving kinetic equations, WHAMP software [Rönmark, 1982] follows the modes that can propagate for given plasma conditions, and it also estimates the wave vector region where the imaginary part of the wave frequency is positive. In the presence of minor ion species, there are stop bands above each ion species gyrofrequency in the case of a parallel

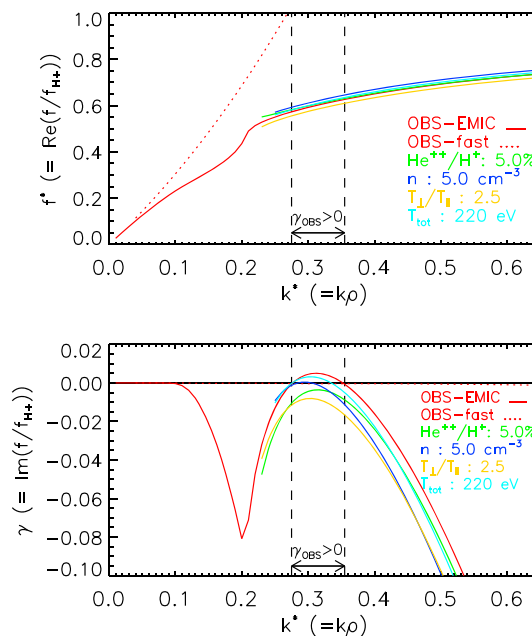


Figure 6. Waves in Homogeneous, Anisotropic Multi-component Plasmas (WHAMP) dispersion relations obtained for locally observed plasma parameters (in red; see Table 3). Results for different plasma parameters are shown in different colors, each color being the result of the change of one parameter, the others being unchanged. On the bottom panel, the line $\gamma = 0$ is plotted in plain black.

propagation [Smith and Brice, 1964]. LH waves cannot propagate in these stop bands. The band wideness is directly connected to the minor specie abundance. In the plasma mantle the numerical studies based on the linear theory focused on the possibility of a local destabilization in the presence of He^+ and O^+ minor species [Engbretson et al., 2012]. In the cusp the studies are made assuming pure proton plasma [Nykyri et al., 2006; Grison et al., 2005].

In the present study we focus on the influence of He^{++} minor species on the wave growth. The inputs are derived from the experimental measurements and presented in Table 3. Populations are modeled as Maxwellian distributions. The dispersion relations are plotted in Figure 6. Top (resp. bottom) panels present the evolution of $f^* = \text{Re}(f/f_{H^+})$ (resp. $\gamma = \text{Im}(f/f_{H^+})$). The fast magnetosonic mode (dotted red line) whose frequency grows very quickly with respect to k^* crosses f_{H^+} for $k^* = 0.27$ (top panel) while its imaginary part (bottom panel) starts at zero and decreases very slowly ($\gamma = -2 \times 10^{-3}$ for $k^* = 0.65$) meaning that the mode is weakly damped over the considered interval. The EMIC mode dispersion relation is drawn in plain red (the polarization is left-hand for the whole dispersion). The frequency increase with respect to k^* is quick up to $k^* = 0.2$, and then the dispersion relation starts an asymptotic approach to f_{H^+} . γ evolution of this mode is more complicated. The first local minimum is seen at $k^* = 0.2$ ($\gamma = -8 \times 10^{-2}$), then γ becomes positive between the two vertical dotted black lines ($k_{min}^* = 0.27$; $k_{max}^* = 0.32$; $\gamma \leq 5 \times 10^{-3}$). The frequency of the local minimum is about $0.5 f_{H^+}$, hence $f_{\text{He}^{++}}$. Waves are damped in this region due to the resonance with solar wind helium particles and the presence of a stop band just above $f_{\text{He}^{++}}$. However, the He^{++} abundance is low enough to allow the LH mode to cross this region. The short interval where wave can be amplified ($\gamma > 0$) contains the experimental k values of the observed electromagnetic waves. This highlights that the waves are locally amplified thanks to the large ion temperature anisotropy and that the observed wave number corresponds to the wave number predicted by the linear theory for a local amplification process.

We performed many calculations with different input parameters. The most representative are plotted on Figure 6. A 10% decrease in T_{\perp}/T_{\parallel} ratio (yellow line) makes the distribution function stable to the anisotropy ($\gamma \leq -10^{-1}$), when a similar decrease of the ion temperature (cyan line) slightly weakens γ . A plasma total density of 5 cm^{-3} (blue line) is the lowest value to get a positive γ value. Finally, a strong increase (by about 50%) of the He^{++} fraction makes the waves being damped. The proton temperature anisotropy is the key parameter for the wave amplification. However, the amplification can be stopped by a small change in the other parameters.

This WHAMP study confirms experimental results (k estimation), and it identifies the proton temperature anisotropy (cf. Figure 3) as the main energy source for the wave amplification process. One can note that the frequency interval $[0.56, 0.63] f_{H^+}$ of $\gamma > 0$ is spanning over the peak frequencies in the spacecraft frame and in the plasma frame (cf. Table 2). The monochromatic aspect of the studied structure is explained by the two regions of strong wave damping due to He^{++} resonance (below) and H^+ resonance (above). The obtained maximal γ value is about 0.5%.

4. Discussion

From the WHAMP simulations we find four major factors that can stop the wave growth: a low proton temperature anisotropy, a low ion temperature, a low total density, and a high He^{++} density. For anisotropy ratio lower than 2.5 or for a He^{++} concentration larger than 5% it is impossible to amplify waves at the considered frequency due to the He^{++} resonance. A higher total temperature or a denser plasma contributes also to a larger γ . Considering that an instrumental effect (overwhelming) can lead CODIF to overestimate the He^{++} density, we looked in the solar wind composition monitored by ACE spacecraft. The He^{++} proportion in the solar wind for this event is usual (2.5–4%) and we state that the same proportion should be found in the cusp. As noted in the observations T_{\perp}/T_{\parallel} is the highest (2.5–3) from 19:32 until 19:42, time at which the reconnection site is switching from dayside to lobeside.

As $f_{\text{He}^{++}}$ increases with the magnetic field intensity, the observed waves should be damped when propagating toward the ionosphere. This might occur in the cusp proper where a significant fraction of the shocked solar wind plasma reaches the ionosphere. However the magnetic field lines mapping the polar mantle are populated only above a certain distance from the Earth. The wave damping at $f_{\text{He}^{++}}$ is

thus not active at low altitudes. Even if EMIC waves can be found in both mantle and cusp proper regions, the absence of He^{++} at low altitudes in the mantle region explains why one can observe on ground ULF signatures 1 or 2° poleward of the cusp (in the mantle region) and none in the cusp region [Engebretson *et al.*, 2009].

The frequency (in the plasma frame) obtained through the WHAMP simulations is higher than the observed one in the spacecraft frame, and it is lower than the observed one in the plasma frame (after the Doppler correction). In the plasma frame, ions with a thermal velocity $v_{th\parallel}$ resonate with waves oscillating at the frequency f_{res} : $f_{res} = f_{H^+} - k_{\parallel}/(2\pi) \times v_{th\parallel}$ [Kennel and Petschek, 1966]. Assuming $k_{\parallel} = 1.0 \times 10^{-2}$ rad/km, the ion parallel temperature of 240 eV measured by CIS corresponds to a resonant frequency of 0.62 Hz or $0.64 f_{H^+}$. This frequency is in the $\gamma > 0$ range of the WHAMP study, and it matches the lowest part of the observed peak frequency range in the spacecraft frame (cf. Table 2). Considering now the k-filtering results (cf. Table 2), the EMIC waves resonate with the [200–570] eV protons. This energy range matches with the lowest part of the ion energy diagram (Figure 3e). Possible explanations for the small discrepancies between observed and simulated frequencies are the plasma description for the WHAMP part (we assumed a Maxwellian distribution, for example) and the uncertainty in the wave vector measurements for the experimental part. The plasma theory suggests that the wave generation is more efficient for a purely parallel propagation. However, from both single and multi-spacecraft observations, a small oblique component is found (15°). This can result from a propagation effect: we show hereafter that the waves traveled more than 10 min to get amplified to the observed level. In the presence of minor ion species (He^+) an increase of the wave angle with propagation has been observed [Young *et al.*, 1981; Rauch and Roux, 1982]. For EMIC waves this angle can quickly increase with the distance from the generation site [Grison *et al.*, 2013].

The energy source for the wave growth is the ion temperature anisotropy of the upward plasma flow. This generation mechanism (temperature anisotropy) agrees with the one proposed in Engebretson *et al.* [2005] for the Pc 1–2 mantle waves. The distribution functions reported in these Polar case studies are stable to the cyclotron instability at a distance from the Earth smaller than in the present case ($\sim 9 R_E$). The direct observation of unstable distribution functions reported in the present study highlights the variability of the plasma properties from one event to another. In the amplification region the waves should propagate along \mathbf{B}_0 in both directions. We noted that the Poynting flux is counterstreaming with respect to the ion flow. This opposite propagation sense of waves and ion flows has already been noted for the mantle waves [Engebretson *et al.*, 2005]. In the present case local amplification factor is $\gamma \times f_{H^+} = 0.05 \text{ s}^{-1}$: to explain the intensity of the narrowband emission, a long duration process is required. This duration t can be estimated from γ and from the total gain in amplitude G with respect to background waves intensity: $G = \exp(\gamma \times t)$. From Figure 3a, we estimate $G \approx 100$, and thus $t \approx 15$ min. Moreover, due to the He^{++} and H^+ resonances, \mathbf{B}_0 has to remain almost constant during that process. We now consider the part of the magnetic field line where the observed EMIC wave frequency (0.6 Hz) is below the H^+ resonance and above the He^{++} resonance. We call d the corresponding length along the field line and we can write $t = d/|\mathbf{v}_w|$ where \mathbf{v}_w is the wave velocity in a rest frame (relative to the Earth). The wave packets propagate with a group velocity \mathbf{v}_g in the plasma frame. We can thus write $\mathbf{v}_w = \mathbf{v}_f + \mathbf{v}_g$ where \mathbf{v}_f stands for the vector of the plasma flow velocity. The absolute value of the wave velocity is thus lower for an opposite propagation to the plasma flow. In the case of a counterstreaming propagation, the waves stay longer in that region and they might be amplified to a higher level. The spacecraft velocity is lower than 5 km/s, and it can thus be neglected. For simplicity we neglect the perpendicular velocities too: $|\mathbf{v}_w| = |\mathbf{v}_{f\parallel} + \mathbf{v}_{g\parallel}|$. We assume $|v_{f\parallel}| \approx 100$ km/s (observed parallel flow velocity) and $|v_{g\parallel}| \approx 200$ km/s (WHAMP results). For the waves propagating parallel to the plasma flow ($|\mathbf{v}_w| \approx 300$ km/s), the process should take place over a distance of $43 R_E$ with an almost constant $|\mathbf{B}_0|$ which is not realistic in the cusp region. For the waves propagating anti-parallel to the plasma flow ($|\mathbf{v}_w| \approx 100$ km/s), the requested length is about $14 R_E$. This is plausible because the field line intensity varies slowly in the region above the spacecraft due to shallow minimum in the region of the “knee” of the polar mantle. These values are only rough estimations, and a full simulation taking into account the field line geometry is beyond the scope of this paper. However, our estimations demonstrate that the intense narrowband emissions and the plasma flow must necessarily be observed streaming in opposite directions: for a given part of the magnetic field line, the amplification level of the waves propagating along the flow is much lower than the amplification level of the counterstreaming waves. The two key factors are the smooth evolution of the magnetic field line intensity above the spacecraft and the reduced absolute wave velocity when the plasma flow and the waves propagate in opposite directions.

Upgoing plasma is detected during almost 10 min (19:32–19:42), while the EMIC emissions last only about 1 min. Looking back at Figure 3a traces of narrowband emissions are seen until 19:38. We can consider that the spacecraft crosses the active amplification region from 19:34 to 19:38. During the intense wave occurrence period the total density value, T_{\perp}/T_{\parallel} and the total ion temperature are high. The lower intensity of the waves observed after 19:36 can be explained in two ways. First, a lower total temperature and a lower density (cf. Figures 3g and 3h) might result in a lower wave growth, as shown in the WHAMP study. Second, the amplification process should last at least 15 min, and it also takes place above the spacecraft. As we have no information about the plasma properties along the field lines, we can suppose that they are less favorable to a large wave growth along the field lines crossed by the spacecraft after 19:36 than before.

The phase shift and the amplitude perturbation caused by the impedance Z between the plasma and the electric antenna have been studied by *Santolik and Parrot* [2000] and by *Parrot et al.* [2001]. Authors demonstrate that the phase and the amplitude of Z are highly variable from one event to another in a [1 kHz; 139 kHz] frequency range. Authors show that these effects are strongly dependent not only on the frequency, but also on the plasma environment. In the present case we assumed that the transfer function of the plasma-antenna interface was $Z=1$ in order to estimate k from the single spacecraft technique. The good agreement between these results, the k -filtering results, and the WHAMP simulations validate the $Z\approx 1$ assumption a posteriori for this frequency range. We can notice that Z might be slightly larger than 1 (1.2 in the present case) as the refractive index analysis provides lower values than the k -filtering analysis and the WHAMP results. This result should be confirmed using more cases under various plasma environments before it can be generalized.

5. Conclusion

We have identified a left-handed polarized monochromatic electromagnetic structure displaying a 0.6–0.7 f_{H^+} frequency in the plasma frame. The wave vector has been estimated both through the single spacecraft analysis (refractive index analysis), and also through the multi spacecraft analysis (k -filtering analysis). The wave vector is mainly parallel, with a propagation angle of $\sim 15^\circ$. Π_{\parallel} and k_{\parallel} directions are both Earthward meaning that the waves are coming from higher altitudes and hence counterstreaming with respect to the plasma flow. The measured $|k|$ value ($\approx 1.2 \times 10^{-2}$ rad/km) is consistent with the WHAMP simulation results: γ is positive for this k value in the local plasma conditions. A good agreement between the single spacecraft and the multi spacecraft analysis makes it possible to state $Z\approx 1$ in order to estimate the wave vector through single spacecraft analysis. We have to confirm this result in the future using more events under various plasma environments as the inner magnetosphere where the EMIC wave number is an important parameter to understand the wave particle interaction processes [*Silin et al.*, 2011].

These emissions are not linked with any simultaneous ion plasma injections neither with velocity shears, as it is usually the case in the cusp region, but with mirrored ions. These waves are identified as Pc 1–2 mantle waves. Even if the waves can be destabilized above and below the spacecraft, only waves that have been already amplified during more than 15 min can be intensified to the observed level (considering $\gamma=0.5\%$). These waves necessarily come from higher regions. Analysis of the full amplification scenario along the magnetic field line is left for a future study. It is worth to notice that waves propagating upward can contribute to the EMIC waves observed in the plasma mantle. The key factor for the wave amplification in the present case is the large T_{\perp}/T_{\parallel} ratio. Then, the locally high plasma density and the He^{++} ion fraction play a significant role, too.

For the first time we report distribution functions unstable to the ion cyclotron instability in the mantle region so close to the Earth. The wave damping at $f_{He^{++}}$ explains why signatures of such waves are observed on ground only poleward of the cusp footprint and not at the cusp footprint itself.

In addition to these EMIC waves we also identified broadband ULF noise detected simultaneously with ion injections. The present case study highlights the variety of the process of wave generation in the distant cusp.

References

- Balogh, A., et al. (2001), The cluster magnetic field investigation: Overview of in-flight performance and initial results, *Ann. Geophys.*, 19, 1207–1217, doi:10.5194/angeo-19-1207-2001.

Acknowledgments

We acknowledge the ESA Cluster Active Archive (CAA), the FGM, PEACE, and CIS teams for supplying the Cluster data. We acknowledge the ACE team for supplying the IMF data and the He^{++} density measurements. We thank JM Bosqued (IRAP) for fruitful discussions on the He^{++} density. We acknowledge support of grants P209/11/P848 and LH12231. We acknowledge G. Belmont (LPP/CNRS), P. Robert (LPP/CNRS), and L. Rezeau (LPP/Univ. Paris 6) for the WHAMP software version used in this study. The research leading to these results has received funding from the European Community's Seventh Framework Programme (FP7-SPACE-2010-1) under grant agreement 284520 (MAARBLE).

M. A. Balikhin thanks three anonymous reviewers for their assistance in evaluating this manuscript.

- Burch, J. L. (1973), Rate of erosion of dayside magnetic flux based on a quantitative study of the dependence of polar cusp latitude on the interplanetary magnetic field, *Radio Sci.*, *8*(11), 955–961, doi:10.1029/RS008i011p00955.
- Carbary, J. F., and C.-I. Meng (1986), Relations between the interplanetary magnetic field Bz, AE index, and cusp latitude, *J. Geophys. Res.*, *91*(A2), 1549–1556, doi:10.1029/JA091iA02p01549.
- Chen, S.-H., S. A. Boardsen, S. F. Fung, J. L. Green, R. L. Kessel, L. C. Tan, T. E. Eastman, and J. D. Craven (1997), Exterior and interior polar cusps: Observations from Hawkeye, *J. Geophys. Res.*, *102*(A6), 11,335–11,347, doi:10.1029/97JA00743.
- Cornilleau-Wehrin, N., et al. (2003), First results obtained by the Cluster STAFF experiment, *Ann. Geophys.*, *21*, 437–456, doi:10.5194/angeo-21-437-2003.
- D'Angelo, N., A. Bahnsen, and H. Rosenbauer (1974), Wave and particle measurements at the polar cusp, *J. Geophys. Res.*, *79*(22), 3129–3134, doi:10.1029/JA079i022p03129.
- Dungey, W. (1961), Interplanetary magnetic field and the auroral zones, *Phys. Rev. Lett.*, *6*, 47–49, doi:10.1103/PhysRevLett.6.47.
- Dyrud, L. P., M. J. Engebretson, J. L. Posch, W. J. Hughes, H. Fukunishi, R. L. Arnoldy, P. T. Newell, and R. B. Horne (1997), Ground observations and possible source regions of two types of Pc 1–2 micropulsations at very high latitudes, *J. Geophys. Res.*, *102*(A12), 27,011–27,027, doi:10.1029/97JA02191.
- Engebretson, M. J., T. G. Onsager, D. E. Rowland, R. E. Denton, J. L. Posch, C. T. Russell, P. J. Chi, R. L. Arnoldy, B. J. Anderson, and H. Fukunishi (2005), On the source of Pc1-2 waves in the plasma mantle, *J. Geophys. Res.*, *110*, A06201, doi:10.1029/2004JA010515.
- Engebretson, M. J., J. Moen, J. L. Posch, F. Lu, M. R. Lessard, H. Kim, and D. A. Lorentzen (2009), Searching for ULF signatures of the cusp: Observations from search coil magnetometers and auroral imagers in Svalbard, *J. Geophys. Res.*, *114*, A06217, doi:10.1029/2009JA014278.
- Engebretson, M. J., et al. (2012), Cluster observations of band-limited Pc 1 waves associated with streaming H⁺ and O⁺ ions in the high-altitude plasma mantle, *J. Geophys. Res.*, *117*, A10219, doi:10.1029/2012JA017982.
- Escoubet, C. P., and J. M. Bosqued (1989), The influence of IMF-Bz and/or AE on the polar cusp: An overview of observations from the AUREOL-3 satellite, *Planet. Space Sci.*, *37*, 609–626, doi:10.1016/0032-0633(89)90100-1.
- Escoubet, C. P., M. Fehringer, and M. Goldstein (2001), The Cluster mission, *Ann. Geophys.*, *19*, 1197–1200, doi:10.5194/angeo-19-1197-2001.
- Escoubet, C. P., et al. (2008), Effect of a northward turning of the interplanetary magnetic field on cusp precipitation as observed by Cluster, *J. Geophys. Res.*, *113*, A07513, doi:10.1029/2007JA012771.
- Escoubet, C. P., et al. (2013), Double cusp encounter by cluster: Double cusp or motion of the cusp?, *Ann. Geophys.*, *31*, 713–723, doi:10.5194/angeo-31-713-2013.
- Frank, L. A. (1971), Plasma in the Earth's polar magnetosphere, *J. Geophys. Res.*, *76*(22), 5202–5219, doi:10.1029/JA076i022p05202.
- Gosling, J. T., M. F. Thomsen, S. J. Bame, R. C. Elphic, and C. T. Russell (1991), Observations of reconnection of interplanetary and lobe magnetic field lines at high-latitude magnetopause, *J. Geophys. Res.*, *96*(A8), 4097–41,106, doi:10.1029/91JA01139.
- Grison, B., F. Sahraoui, B. Lavraud, T. Chust, N. Cornilleau-Wehrin, H. Rème, A. Balogh, and M. André (2005), Wave particle interactions in the high-altitude polar cusp: A cluster case study, *Ann. Geophys.*, *23*, 3699–3713, doi:10.5194/angeo-23-3699-2005.
- Grison, B., O. Santolik, N. Cornilleau-Wehrin, A. Masson, M. J. Engebretson, J. S. Pickett, Y. Omura, P. Robert, and R. Nomura (2013), EMIC triggered chorus emissions in cluster data, *J. Geophys. Res. Space Physics*, *118*, 1159–1169, doi:10.1002/jgra.50178.
- Gustafsson, G., et al. (2001), First results of electric field and density observations by Cluster EFW based on initial months of operation, *Ann. Geophys.*, *19*, 1219–1240, doi:10.5194/angeo-19-1219-2001.
- Heikkila, W. J., and J. D. Winningham (1971), Penetration of magnetosheath plasma to low altitudes through the dayside magnetospheric cusps, *J. Geophys. Res.*, *76*(4), 883–891, doi:10.1029/JA076i004p00883.
- Horne, R. B., and R. M. Thorne (1993), On the preferred source location for the convective amplification of ion cyclotron waves, *J. Geophys. Res.*, *98*(A6), 9233–9247, doi:10.1029/92JA02972.
- Jacobs, J. A., Y. Kato, S. Matsushita, and V. A. Troitskaya (1964), Classification of geomagnetic micropulsations, *J. Geophys. Res.*, *69*(1), 180–181, doi:10.1029/JZ069i001p00180.
- Johnstone, A. D., et al. (1997), PEACE: A plasma electron and current experiment, *Space Sci. Rev.*, *79*, 351–398, doi:10.1023/A:1004938001388.
- Kennel, C. F., and H. E. Petschek (1966), Limit on stably trapped particle fluxes, *J. Geophys. Res.*, *71*(1), 1–28, doi:10.1029/JZ071i001p00001.
- Lavraud, B., et al. (2002), Cluster observations of the exterior cusp and its surrounding boundaries under northward IMF, *Geophys. Res. Lett.*, *29*(20), 1995, doi:10.1029/2002GL015464.
- Lavraud, B., et al. (2004), The exterior cusp and its boundary with the magnetosheath: Cluster multi-event analysis, *Ann. Geophys.*, *22*, 3039–3054, doi:10.5194/angeo-22-3039-2004.
- Lavraud, B., et al. (2005), High-altitude cusp flow dependence on IMF orientation: A 3-year Cluster statistical study, *J. Geophys. Res.*, *110*, A02209, doi:10.1029/2004JA010804.
- Le, G., X. Blanco-Cano, C. T. Russell, X.-W. Zhou, F. Mozer, K. J. Trattner, S. A. Fuselier, and B. J. Anderson (2001), Electromagnetic ion cyclotron waves in the high altitude cusp: Polar observations, *J. Geophys. Res.*, *106*(A9), 19,067–19,079, doi:10.1029/2000JA900163.
- Liao, J., L. M. Kistler, C. G. Mouikis, B. Klecker, I. Dandouras, and J.-C. Zhang (2010), Statistical study of O⁺ transport from the cusp to the lobes with Cluster CODIF data, *J. Geophys. Res.*, *115*, A00J15, doi:10.1029/2010JA015613.
- McComas, D. J., S. J. Bame, P. Barker, W. C. Feldman, J. L. Phillips, P. Riley, and J. W. Griffiee (1998), Solar wind electron proton alpha monitor (SWEPAM) for the Advanced Composition Explorer, *Space Sci. Rev.*, *86*, 563–612, doi:10.1023/A:1005040232597.
- Menk, F. W., B. J. Fraser, H. J. Hansen, P. T. Newell, C. I. Meng, and R. J. Morris (1992), Identification of the magnetospheric cusp and cleft using Pc 1–2 pulsations, *J. Atmos. Sol. Terr. Phys.*, *54*, 1021–1042, doi:10.1016/0021-9169(92)90069-W.
- Newell, P. T., and C.-I. Meng (1992), Mapping the dayside ionosphere to the magnetosphere according to particle precipitation characteristics, *Geophys. Res. Lett.*, *19*(6), 609–612, doi:10.1029/92GL00404.
- Nykyri, K., P. J. Cargill, E. A. Lucek, T. S. Horbury, A. Balogh, B. Lavraud, I. Dandouras, and H. Rème (2003), Ion cyclotron waves in the high altitude cusp: CLUSTER observations at varying spacecraft separations, *Geophys. Res. Lett.*, *30*(24), 2263, doi:10.1029/2003GL018594.
- Nykyri, K., et al. (2004), Cluster observations of magnetic field fluctuations in the high-altitude cusp, *Ann. Geophys.*, *22*, 2413–2429, doi:10.5194/angeo-22-2413-2004.
- Nykyri, K., B. Grison, P. J. Cargill, B. Lavraud, E. Lucek, I. Dandouras, A. Balogh, N. Cornilleau-Wehrin, and H. Rème (2006), Origin of the turbulent spectra in the high-altitude cusp: Cluster spacecraft observations, *Ann. Geophys.*, *24*, 1057–1075, doi:10.5194/angeo-24-1057-2006.
- Parrot, M., F. Lefevre, J. L. Rauch, O. Santolik, and M. M. Mogilevski (2001), Propagation characteristics of auroral kilometric radiation observed by the MEMO experiment on Interball 2, *J. Geophys. Res.*, *106*(A1), 315–325, doi:10.1029/2000JA900072.

- Pinçon, J. L., and F. Lefeuvre (1991), Local characterization of homogeneous turbulence in a space plasma from simultaneous measurements of field components at several points in space, *J. Geophys. Res.*, *96*(A2), 1789–1802, doi:10.1029/90JA02183.
- Pinçon, J. L., and U. Motschmann (1998), Multispacecraft filtering: General framework, in *Analysis Methods for Multi-spacecraft Data*, pp. 65–78, International Space Science Institute, Bern, Switzerland.
- Pitout, F., C. P. Escoubet, Y. V. Bogdanova, E. Georgescu, A. N. Fazakerley, and H. Rème (2006a), Response of the mid-altitude cusp to rapid rotations of the IMF, *Geophys. Res. Lett.*, *33*, L11107, doi:10.1029/2005GL025460.
- Pitout, F., C. P. Escoubet, B. Klecker, and H. Rème (2006b), Cluster survey of the mid-altitude cusp: 1. Size, location, and dynamics, *Ann. Geophys.*, *24*, 3011–3026, doi:10.5194/angeo-24-3011-2006.
- Rauch, J. L., and A. Roux (1982), Ray tracing of ulf waves in a multicomponent magnetospheric plasma: Consequences for the generation mechanism of ion cyclotron waves, *J. Geophys. Res.*, *87*(A10), 8191–8198, doi:10.1029/JA087iA10p08191.
- Reiff, P. H., R. W. Spiro, and J. L. Burch (1980), Cusp proton signatures and the interplanetary magnetic field, *J. Geophys. Res.*, *85*(A11), 5997–6005, doi:10.1029/JA085iA11p05997.
- Rème, H., et al. (2001), First multispacecraft ion measurements in and near the Earth's magnetosphere with the identical Cluster ion spectrometry (CIS) experiment, *Ann. Geophys.*, *19*, 1303–1354, doi:10.5194/angeo-19-1303-2001.
- Rönnmark, K. (1982), Waves in homogeneous, anisotropic multicomponent plasmas (WHAMP), *Kiruna Geophys. Inst. Rep.* 179, Kiruna Geophys. Inst., Kiruna, Sweden.
- Rosenbauer, H., H. Gruenwaldt, M. D. Montgomery, G. Paschmann, and N. Skopke (1975), HEOS-2 plasma observations in the distant polar magnetosphere: The plasma mantle, *J. Geophys. Res.*, *80*(19), 2723–2737, doi:10.1029/JA080i019p02723.
- Russell, C. T. (2000), POLAR eyes the cusp, in *Proc. of the Cluster II Workshop: Multiscale/Multipoint Plasma Measurements*, p. 47, Imperial College, London, U. K. ESA SP-449.
- Russell, C. T., C. R. Chappell, M. D. Montgomery, M. Neugebauer, and F. L. Scarf (1971), Ogo 5 observations of the polar cusp on November 1, 1968, *J. Geophys. Res.*, *76*(28), 6743–6764, doi:10.1029/JA076i028p06743.
- Sahraoui, F., et al. (2003), ULF wave identification in the magnetosheath: The k-filtering technique applied to Cluster II data, *J. Geophys. Res.*, *108*(A9), 1335, doi:10.1029/2002JA009587.
- Santolik, O., and M. Parrot (2000), Application of wave distribution function methods to an ELF hiss event at high latitudes, *J. Geophys. Res.*, *105*(A8), 18,885–18,894, doi:10.1029/2000JA900029.
- Santolik, O., F. Lefeuvre, M. Parrot, and J. L. Rauch (2001), Complete wave-vector directions of electromagnetic emissions: Application to INTERBALL-2 measurements in the nightside auroral zone, *J. Geophys. Res.*, *106*(A7), 13,191–13,201, doi:10.1029/2000JA000275.
- Santolik, O., M. Parrot, and F. Lefeuvre (2003), Singular value decomposition methods for wave propagation analysis, *Radio Sci.*, *38*(1), 1010, doi:10.1029/2000RS002523.
- Scarf, F. L., R. W. Fredricks, I. M. Green, and C. T. Russell (1972), Plasma waves in the dayside polar cusp: 1, Magnetospheric observations, *J. Geophys. Res.*, *77*(13), 2274–2293, doi:10.1029/JA077i013p02274.
- Silin, I., I. R. Mann, R. D. Sydora, D. Summers, and R. L. Mace (2011), Warm plasma effects on electromagnetic ion cyclotron wave MeV electron interactions in the magnetosphere, *J. Geophys. Res.*, *116*, A05215, doi:10.1029/2010JA016398.
- Smith, C. W., J. L'Heureux, N. F. Ness, M. H. Acuna, L. F. Burlaga, and J. Scheifele (1998), The ACE Magnetic Fields Experiment, *Space Sci. Rev.*, *86*, 613–632, doi:10.1023/A:1005092216668.
- Smith, R. L., and N. Brice (1964), Propagation in multicomponent plasmas, *J. Geophys. Res.*, *69*(23), 5029–5040, doi:10.1029/JZ069i023p05029.
- Sundkvist, D., V. Krasnoselskikh, P. K. Shukla, A. Vaivads, M. André, S. Buchert, and H. Rème (2005a), In situ multi-satellite detection of coherent vortices as a manifestation of Alfvénic turbulence, *Nature*, *436*, 825–828, doi:10.1038/nature03931.
- Sundkvist, D., et al. (2005b), Multi-spacecraft determination of wave characteristics near the proton gyrofrequency in high-altitude cusp, *Ann. Geophys.*, *23*, 983–995, doi:10.5194/angeo-23-983-2005.
- Tsyganenko, N. A. (1989), A magnetospheric magnetic field model with a warped tail current sheet, *Planet. Space Sci.*, *37*, 5–20, doi:10.1016/0032-0633(89)90066-4.
- Vontrat-Reberac, A., J. M. Bosqued, M. G. G. Taylor, B. Lavraud, D. Fontaine, M. W. Dunlop, H. Laakso, N. Cornilleau-Werhlin, P. Canu, and A. Fazakerley (2003), Cluster observations of the high-altitude cusp for northward interplanetary magnetic field: A case study, *J. Geophys. Res.*, *108*(A9), 1346, doi:10.1029/2002JA009717.
- Young, D. T., S. Perraut, A. Roux, C. de Villedary, R. Gendrin, A. Korth, G. Kremser, and D. Jones (1981), Wave-particle interactions near He⁺ observed on GEOS 1 and 2. I - Propagation of ion cyclotron waves in He⁺ rich plasma, *J. Geophys. Res.*, *86*(A8), 6755–6772, doi:10.1029/JA086iA08p06755.